Title

Revisiting the conversion reaction voltage and the reversibility of the CuF2 electrode in Li-ion batteries

Journal

Nano Research, 10(12)

ISSN

1998-0124

Authors

Seo, Joon Kyo
Cho, Hyung-Man
Takahara, Katsunori
et al.

Publication Date

2017-12-01

DOI

10.1007/s12274-016-1365-6

Peer reviewed

Nano Research
DOI 10.1007/s12274-016-1365-6
Research Article
ISSN 1998-0124
CN 11-5974/O4

Revisiting the conversion reaction voltage and the reversibility of the CuF_2 electrode in Li-ion batteries

Joon Kyo Seo[1,2], Hyung-Man Cho[1,2], Katsunori Takahara[1], Karena W. Chapman[3], Olaf J. Borkiewicz[3], Mahsa Sina[1] (✉), and Y. Shirley Meng[1,2] (✉)

[1] *Department of NanoEngineering, University of California San Diego, 9500 Gilman Drive, La Jolla, CA 92093, USA*
[2] *Materials Science and Engineering, University of California San Diego, 9500 Gilman Drive, La Jolla, CA 92093, USA*
[3] *X-ray Science Division, Advanced Photon Source, Argonne National Laboratory, 9700 South Cass Avenue, Argonne, IL 60439, USA*

Received: 20 September 2016
Revised: 31 October 2016
Accepted: 9 November 2016

KEYWORDS
Li-ion battery,
conversion material,
reaction voltage,
nanoparticle,
reversibility,
coating

ABSTRACT

Deviation between thermodynamic and experimental voltages is one of the key issues in Li-ion conversion-type electrode materials; the factor that affects this phenomenon has not been understood well in spite of its importance. In this work, we combine first principles calculations and electrochemical experiments with characterization tools to probe the conversion reaction voltage of transition metal difluorides MF_2 (M = Fe, Ni, and Cu). We find that the conversion reaction voltage is heavily dependent on the size of the metal nanoparticles generated. The surface energy of metal nanoparticles appears to penalize the reaction energy, which results in a lower voltage compared to the thermodynamic voltage of a bulk-phase reaction. Furthermore, we develop a reversible CuF_2 electrode coated with NiO. Electron energy loss spectroscopy (EELS) elemental maps demonstrate that the lithiation process mostly occurs in the area of high NiO content. This suggests that NiO can be considered a suitable artificial solid electrolyte interphase that prevents direct contact between Cu nanoparticles and the electrolyte. Thus, it alleviates Cu dissolution into the electrolyte and improves the reversibility of CuF_2.

1 Introduction

Lithium-ion batteries have been used as energy sources in various mobile and stationary applications. In order to meet the growing demand for mass-market adoption, substantial improvement in energy density and reduction in the cost of rechargeable batteries are crucial [1]. Conversion materials have a higher Li-storage capacity than commercialized intercalation electrode compounds [2]. Among conversion materials, transition metal difluorides MF_2(M = Fe, Ni, Cu), especially show a relatively higher reaction voltage due to the strong M–F ionic bond [3]. In order to achieve the potential implication of these compounds

Address correspondence to Y. Shirley Meng, shmeng@ucsd.edu; Mahsa Sina, msina@ucsd.edu

in rechargeable batteries, wide progress has been made. Badway et al. developed a carbon-metal fluoride nanocomposite composed of nano-domains of FeF_3 with a high surface-to-volume ratio in a carbon matrix. It was demonstrated that the high surface-to-volume ratio of nano-sized FeF_3 are electroactively improved [4, 5]. Later, they introduced another concept of nanocomposite design that enables CuF_2 to have 98% of the theoretical discharge capacity within the voltage range 2.0–4.0 V vs. Li/Li^+. The nanocomposite composed of a carbon matrix with intercalation compounds (e.g., MoO_3, V_2O_5, and MnS_2) promoted electron and ion conductivity [6]. Oxygen doping into metal fluorides, such as FeOF and Fe_2OF_4, has also been shown to enhance electrochemical properties [7–10]. It is proposed that the substitution of O for F increases the average conversion voltage and facilitates cycling stability by incorporating more covalent M–O bonds into the ionic fluoride structure. Recently, Wang et al. reported reversible binary metal fluorides $Cu_yFe_{1-y}F_2$ [11]. They proposed the incorporation of Cu into the FeF_2 crystal lattice, which promotes the reversible redox behavior $Cu^{2+} \leftrightarrow Cu^0$. Even though the reversible capacity of Cu content degrades due to dissolution of Cu, the binary fluoride exhibits low hysteresis with high voltage and capacity.

Despite progresses in conversion materials as promising materials for future batteries, there are still unsolved issues: (i) the discrepancy between the experimental voltage of transition metal difluorides, $MF_2(M = Fe, Ni, Cu)$ and the theoretical thermodynamic voltage, and (ii) the non-reversible conversion reaction of CuF_2. As for the voltage discrepancy, it has been reported that the experimental voltage plateau for $MF_2(M = Fe, Ni, Cu)$ is lower than the thermodynamic reaction voltage [12, 13]. In order to understand the origin of the voltage deviation, we used density functional theory (DFT) and calculated the conversion reaction voltage depending on the size of the $M(M = Fe, Ni, Cu)$ nanoparticle formed during discharge. We also conducted a PITT experiment on NiF_2 and CuF_2 electrodes to observe near-equilibrium conversion reaction voltages. The average sizes of Ni and Cu nanoparticles during lithiation were measured by scanning transmission electron microscopy (STEM) to correlate the nano-size effect of metal particle formation with the reaction voltages.

The CuF_2 electrode has the highest theoretical voltage among $MF_2(M = Fe, Ni, Cu)$ species, which is suitable for power-driven mobile devices; however, CuF_2 is intrinsically non-reversible in contrast to FeF_2 and NiF_2 [14, 15]. Wang et al. reported that the origin of irreversibility is due to the separation between relatively large Cu nanoparticles (5–12 nm in diameter) and LiF, which blocks electron paths [14]. Yamakawa et al. suggested that the different diffusivities of the ionic phases (F^- and Li^+) bring about the formation of an LiF coating on the CuF_2/Cu and CuF_2/electrolyte interfaces and hinders the reversible reaction [16]. Recently, Hua et al. reported that the degradation mechanism of CuF_2 is associated with Cu dissolution along with LiF consumption [17]. In this study, we apply a NiO coating on CuF_2 to study the effect of NiO on the reversible CuF_2 conversion reaction. As NiO is not electrochemically active within our voltage range (2.0–4.0 V), it does not contribute additional capacity to CuF_2. This is opposed to the cases of other metal oxides such as MoO_3, V_2O_5, and MnS_2 that have been adopted to the CuF_2 conversion reaction [6]. ADF-STEM and electron energy loss spectroscopy (EELS) were used to suggest a reversible conversion mechanism for the NiO-coated CuF_2 electrode.

2 Experimental

2.1 Computational methodology

We conducted first principles calculations [18] based on spin-polarized GGA and GGA + *U* [19, 20] using the Perdew–Burke–Ernzerhof exchange and correlation functionals [21]. We used a plane-wave basis set and the projector-augmented wave (PAW) method [22, 23] as parameterized in the Vienna *ab initio* simulation package (VASP) [24]. A gamma point mesh is performed with 9 × 7 × 7 *k*-points for CuF_2, 7 × 7 × 11 *k*-points for NiF_2, and 7 × 7 × 9 *k*-points for FeF_2. For metal nanoparticles, gamma point was used to sample the Brillouin zone, and periodic boundary conditions were imposed on the unit cell where vacuum size was larger than the nanoparticle diameter to prohibit interactions between the images. All the atoms were fully relaxed to calculate the optimized structure

with a cutoff energy of 1.3 times the maximum cutoff specified by the pseudopotentials on a plane wave basis set. Our GGA + *U* calculations indicate that the lattice parameters of metal fluorides agreed well with experimental measurements and the error is less than 2% (Table S1 in the Electronic Supplementary Material (ESM)). It is noted that we adopted a mixed GGA and GGA + *U* framework as proposed by Jain et al. [25] in order to obtain accurate reaction energy and voltage of conversion reaction. The detailed explanation of the framework is discussed in the results and discussion section.

2.2 Material preparation

Commercial CuF_2 (Aldrich) and NiF_2 (Alfa Aesar) powders were used for this study. In order to synthesize carbon coated with metal difluoride, CuF_2/C (or NiF_2/C), we prepared a milling jar where 80 wt.% of conversion material and 20 wt.% of acetylene black (Strem Chemicals) were mixed together in an MBraun Ar-filled glovebox (H_2O < 0.1 ppm). The jar was sealed with Parafilm before being transferred to a planetary ball mill (PM 100, Retsch) and the milling was performed for 6 hours at 500 rpm. In addition, NiO (Aldrich) coated CuF_2 (NiO-CuF_2) with the composition CuF_2: NiO = 85:15 w/w was prepared by ball milling for 4 hours at 650 rpm under an Ar atmosphere. NiO-CuF_2 was milled again with acetylene black to synthesize carbon-coated samples (NiO-CuF_2/C). The mass loadings of CuF_2 and NiF_2 in the PITT discharge experiment were 1.36 and 1.49 mg·cm^{-2}, respectively. Considering the cycling test of CuF_2 and NiO-CuF_2, 0.84 and 1.17 mg·cm^{-2} of CuF_2 were used.

2.3 Material characterizations

The electrochemical cells were disassembled in an argon-filled glovebox, and the electrodes were washed with dimethylene carbonate (DMC). The electrodes were scraped to produce a fine powder. A small amount of powder was placed on a transmission electron microscopy (TEM) lacy carbon film supported on a copper grid. Selected area electron diffraction (SAED) patterns, ADF-STEM images, and EELS were acquired using a JEOL 2010F operated at 197 kV and equipped with a Gatan GIF 200 spectrometer. The EELS spectra were obtained with a collection half angle of 27 mrad and convergence angle of 10 mrad (with an energy resolution of 0.9 eV). Additionally, the ADF-STEM image as an EELS spectrum image was attained using a TEAM 0.5 aberration-corrected instrument operating at 80 kV at Lawrence Berkeley National Laboratory, equipped with a high brightness Schottky-field emission electron source. The ADF-STEM image and EELS elemental maps were acquired using a Gatan Efinia spectrometer with a collection angle of 52 mrad and convergence angle of 30 mrad. Cu dissolution into the electrolyte was characterized by inductively coupled plasma optical emission spectroscopy (ICP-OES) (PerkinElmer Plasma 3700). The electrolyte (25 μL) was gathered from a custom-made electrochemical cell and included into a 25 mL solution matrix (1:1 w/w, HNO_3/HCl). Therefore, the electrolyte was examined at a 1,000-fold dilution [26].

2.4 Electrochemical characterization

Electrochemical characterization was performed using coin-type (2016) cells. We used a battery cycler (Arbin) at room temperature. We made working electrodes composed of active materials (NiO-CuF_2/C, CuF_2/C or NiF_2/C), acetylene black, and polyvinylidene fluoride (PVDF) with a 70:20:10 w/w ratio. Pure lithium metal was used as counter electrode and polypropylene C480 (Celgard) was used as the separator. The coin cells were assembled with the electrolyte consisting of 1 M $LiPF_6$ dissolved in EC and DMC at a weight ratio of 1:1 (BASF) in an MBraun Ar-filled glovebox (H_2O < 0.1 ppm). The theoretical specific capacities of CuF_2 and NiF_2 are 528 and 554 mAh·g^{-1}, respectively, which are used to set the *C* rate. PITT was adopted on the first discharge of CuF_2/C and NiF_2/C cells with the voltage limits of 2.0 and 1.0 V, respectively. The voltage step size was 10 mV with a cut-off current density of *C*/1,000 of active material. In addition, electrochemical cycling of NiO-CuF_2/C and CuF_2/C were tested with the constant current density of C/35. The cell voltage range of 2.0–4.0 V was applied. The first discharge of CuF_2/C and NiF_2/C were performed with the constant current density of *C*/35, and the discharge voltage limit of 2.0 and 1.0 V, respectively. For the linear potential sweep voltammogram, Cu

foil was employed as the working electrode. Other conditions including a coin-type cell, a separator, electrolyte, and a reference electrode were the same as the battery experiments. The scan rate was 1 $mV \cdot s^{-1}$.

3 Results and discussion

3.1 Computational model systems

We set up four different sizes of metal nanoparticle models, $M_n^{\text{cubo or icosa}}$ (n is the number of atoms in the nanoparticle), as shown in Figs. 1(a) and 1(b), in order to calculate the conversion voltage of MF_2 (M = Fe, Ni, Cu), with respect to the metal nanoparticle size

(i) $M_{13}^{\text{cubo or icosa}}$ (13 atoms and ~0.5 nm in diameter),

(ii) $M_{55}^{\text{cubo or icosa}}$ (55 atoms and 0.9–1.0 nm in diameter),

(iii) $M_{147}^{\text{cubo or icosa}}$ (147 atoms and 1.4–1.5 nm in diameter), and

(iv) $M_{309}^{\text{cubo or icosa}}$ (309 atoms and 1.9–2.0 nm in diameter).

The average distance between two diametrically opposed vertices is defined to be the size of a nanoparticle and its radius is listed in Table S2 in the ESM. The shapes of the nanoparticles are ideal cuboctahedron and icosahedron structures, solely consisting of (111) and (100) planes [27], and a (111) plane [28], respectively. These planes correspond to the low Miller index planes with low surface energies [29] resulting in an optimal configuration (cuboctahedron and icosahedron) with minimal total free energy for a given particle size [30–33]. These morphologies are quite similar to the "magic number" nanoparticles, which also have been found to be thermodynamically stable [27, 34]. Because the activation energy to transform morphology among ultra-small nanoparticles is very small [35, 36], our model structures can be converted to different structures. This effect is outside the scope of the present study.

The metal difluorides investigated in our study are FeF_2, NiF_2, and CuF_2 (Fig. 1(c)). These crystals have rutile-type structure where the transition metal atoms are surrounded by 6 fluorine atoms. CuF_2 crystallizes in the monoclinic structure (P 1 21/n 1 space group) that produces a highly distorted octahedron. NiF_2 and FeF_2, however, have a tetragonal structure with P 42/m n m space group.

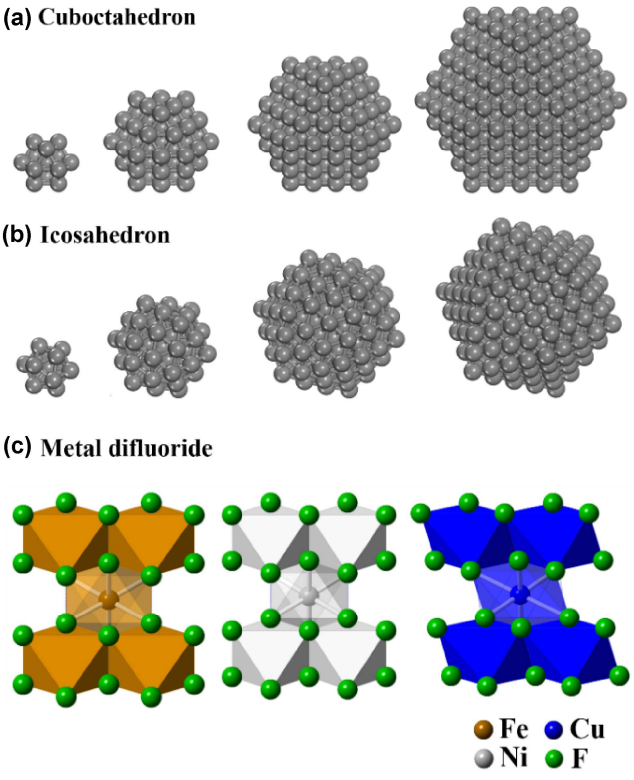

Figure 1 Model systems of (a) cuboctahedron and (b) icosahedron for Fe, Ni, and Cu, composed of 13, 55, 147, and 309 atoms (Fe cuboctahedron: 0.5, 1.0, 1.4, and 2.0 nm in diameter; Fe icosahedron: 0.5, 1.0, 1.4, and 1.9 nm in diameter; Ni cuboctahedron: 0.5, 1.0, 1.5, and 1.9 nm in diameter; Ni icosahedron: 0.5, 0.9, 1.4, and 1.9 nm in diameter; Cu cuboctahedron: 0.5, 1.0, 1.5, and 2.0 nm in diameter; Cu icosahedron: 0.5, 1.0, 1.5, and 1.9 nm in diameter). (c) The crystal structures of FeF_2, NiF_2, and CuF_2. FeF_2 and NiF_2 are tetragonal, and CuF_2 is the monoclinic.

3.2 Influence of metal-nanoparticle size on the conversion reaction voltage

The electrochemical conversion of transition metal difluorides MF_2 (M = Fe, Ni, Cu) with Li is the two-electron reaction where the divalent metal ion is reduced to the metallic phase.

$$MF_2 + 2Li \xrightarrow{2e^-} 2LiF + M \quad (1)$$

The thermodynamic voltage ($E_{\text{thermodynamic}}^{\text{bulk}}$) for the reaction (Eq. (1)) can be obtained from [12]

$$E_{\text{thermodynamic}}^{\text{bulk}} = \frac{G_f(2LiF) - G_f(MF_2)}{-2F} \quad (2)$$

where G_f and F are the standard Gibbs free energy of formation from thermodynamic tables and the Faraday

constant, respectively. It is noted that G_f relates to the bulk-phase formation energy so that $E^{bulk}_{thermodynamic}$ acquired from G_f corresponds to the conversion voltage for the bulk-phase reaction. Most experimental reports on $MF_2(M = Fe, Ni, Cu)$ conversion reactions, however, show that the experimental voltage is much lower than $E^{bulk}_{thermodynamic}$, by up to ~1.5 V [6, 13–16, 37, 38]. Interestingly, the discharge reaction does not generate bulk-phase metal. It is reported that bulk MF_2 is reduced to nanoscale M particles (⩽10 nm) at the first discharge [14–16, 37, 38]. The origin of metal nanoparticle formation is estimated to be the tunneling of electrons from the carbon conductor to the inside of poorly conductive MF_2 and forms M nanoparticles [16].

In order to understand the influence of metal nanoparticle formation on the conversion voltage using DFT, we replaced the bulk metal (M) in Eq. (1) with a metal nanoparticle composed of n atoms $(M_n^{cubo\ or\ icosa})$

$$n \cdot MF_2 + n \cdot 2Li \xrightarrow{n \cdot 2e^-} n \cdot 2LiF + M_n^{cubo\ or\ icosa} \quad (3)$$

where MF_2, Li, and LiF are bulk-phase forms. Then, we adopted the framework of mixing GGA and GGA + U proposed by Jain et al. [25]. This method connects GGA and GGA + U energies, which are reasonable methods to calculate the ground state properties of materials for delocalized electronic states (e.g., metal and LiF) and localized electronic states of d orbitals (e.g., transition metal difluorides), respectively [39]. The computational cell voltage (E^{nano}) is obtained as

$$E^{nano} = \frac{\left\{\left[n \cdot G^{GGA}(2LiF) + G^{GGA}(M_n^{cubo\ or\ icosa})\right] - \left[n \cdot G^{GGA+U}_{renorm}(MF_2) + n \cdot G^{GGA}(2Li)\right]\right\}}{-2n} \quad (4)$$

$G^{GGA+U}_{renorm}(MF_2)$ is calculated as $G^{GGA+U}(MF_2) - \Delta E_M \cdot \Delta E_M$ connects GGA with GGA + U schemes and we adopted 1.723, 2.164, and 1.156 eV for Fe, Ni, and Cu (per atom), when U are 4.0, 6.0, and 4.0 for Fe, Ni, and Cu, respectively [25]. In order to confirm that the mixing framework is suitable for our calculations, we present the comparison of the bulk-phase reaction voltage (Table S3 in the ESM) measured from the GGA method, mixed GGA/GGA + U method, and the tabulated Gibbs free energy of formation [40]. The voltage from the mixed GGA/GGA + U method shows <0.09 V difference with respect to the voltage measured from the thermodynamic table.

We find that E^{nano} for transition metal difluorides (FeF_2, NiF_2, and CuF_2) is lower than $E^{bulk}_{thermodynamic}$ as shown in Fig. 2(a).

The voltage discrepancy between E^{nano} and $E^{bulk}_{thermodynamic}$ is 0.19–1.02 V for metal nanoparticles sized ⩽ 2 nm. This low voltage on formation of metal nanoparticles resembles the conversion voltage measured from experiments, which also exhibits a lower value than the thermodynamic voltage. Ko et al. displayed that the conversion voltage at the first discharge was evaluated to be 1.84 V which is lower than the thermodynamic voltage (2.66 V) on the lithiation reaction of FeF_2 (very slow C rate, approximately C/1,000) [13]. Another study using the

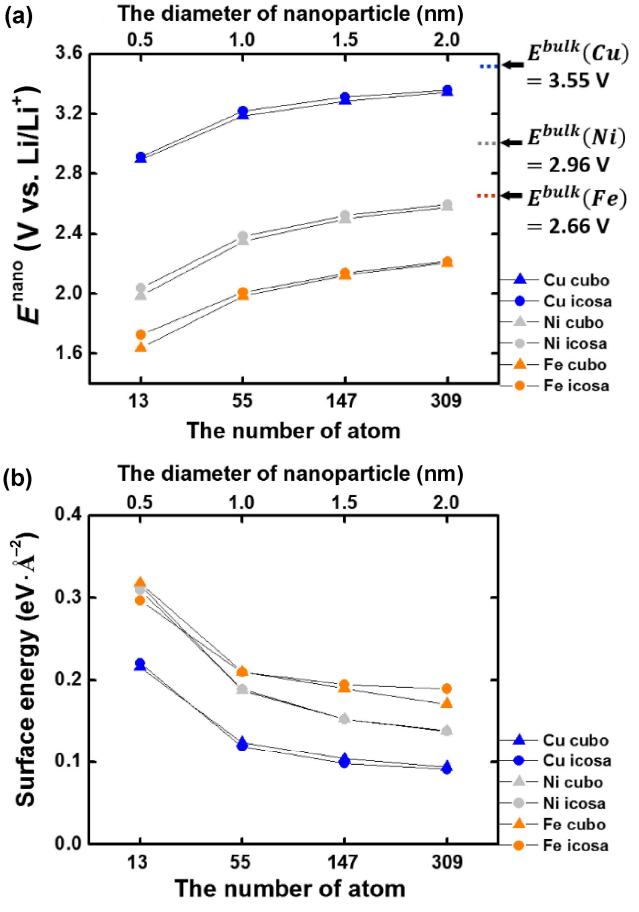

Figure 2 (a) Calculated conversion reaction voltage as a function of the size of M nanoparticle (M = Fe,Ni and Cu) formed. (b) Surface energy of M nanoparticle as a function of its size. The lower x-axis represents the number of atom contained in metal nanoparticle. The upper x-axis is the nanoparticle size in diameter which is approximate value. Detailed size information is demonstrated in Table S2 in the ESM.

galvanostatic intermittent titration technique (GITT) on the conversion reaction of FeF_3 presented a voltage difference [41]. The second plateau (2.36 V) corresponds to the reduction of Fe^{2+} to Fe, which is lower than the thermodynamic voltage. The voltage discrepancy is also commonly found in transition metal oxide cathode materials while nanoscale metal particles are formed during lithiation [42, 43]. Since the experimental voltage is measured from a distribution of nano-sized metal nanoparticles when they were formed, it is impractical to directly compare the average experimental voltage to the calculated voltage at a certain size of metal particle. It is clear, however, that calculation supports the idea that the formation of metal nanoparticles during the conversion reaction could have a lower voltage compared to the thermodynamic voltage of the bulk-phase reaction.

In addition, our computational results indicate that particle size growth leads to increasing E^{nano}. E^{nano} approaches $E^{\text{bulk}}_{\text{thermodynamic}}$ when the particle size is larger than 2 nm (Fig. 2(a)) because the nanoscale property of the metal resembles the bulk metal property as the particle size increases. It is reported that when the metal particle gets larger, the integrity of the metal nanoparticle stabilizes because its Gibbs energy per atom decreases (or increment in cohesive energy), and eventually reaches the stability of the bulk metal [27]. This thermodynamic property is associated with Eq. (4) that Gibbs energy of $\mathrm{M}_n^{\text{cubo or icosa}}$ per atom approaches more negative values when the particle size increases and results in the increment of E^{nano} In our calculations, we did not presume LiF to be a nano-sized phase because LiF is typically a bulk matrix in which metal nanoparticles are distributed.

Importantly, our results also attribute the lower conversion reaction voltage to the surface energy of the metal nanoparticle ($G^{\text{nano}}_{\text{surface}}$). The surface energy as an energy penalty toward the reaction energy needs to be provided to the metal nanoparticle to form during the conversion reaction. We calculated the surface energy of the M nanoparticle ($\mathrm{M} = \mathrm{Fe}, \mathrm{Ni}, \mathrm{Cu}$) as a function of its size [44]

$$G^{\text{nano}}_{\text{surface}} = \frac{G^{\text{GGA}}(\mathrm{M}_n^{\text{cubo or icosa}}) - n \cdot G^{\text{GGA}}(\mathrm{M})}{4\pi r^2} \quad (5)$$

where $G^{\text{GGA}}(\mathrm{M}_n^{\text{cubo or icosa}})$ and $G^{\text{GGA}}(\mathrm{M})$ are the Gibbs energy of an M nanoparticle composed of n atoms and M bulk metal per atom ($\mathrm{M} = \mathrm{Fe}, \mathrm{Ni}, \mathrm{Cu}$), respectively. r is the average radius which is measured by the distance between the center and vertex atoms of a relaxed nanoparticle (Table S2 in the ESM). It is noted that the surface energy increases as the nanoparticle size decreases (Fig. 2(b)), which results in decrease of the reaction energy and affects the reduction of conversion reaction voltage (Fig. 2(a)). This trend is correlated with the fact that while the particle gets smaller, the fraction of thermodynamically unstable surface atoms increases with respect to the fraction of relatively stable bulk atoms. The cuboctahedron consisting of 309 atoms has 108 atoms (35%) on the surface. As the size decreases, the fraction of surface atoms increases to 92% for the cuboctahedron with 13 atoms. We systematically show the energy penalty in the conversion reaction associated with the formation of metal nanoparticles by first principles, which was conceptually discussed by Cabana et al. [2]. Although the surface energy of nanoparticles is primarily studied in our work, other factors including the crystallinity of the material [45], interfacial energy [46, 47], and electronic conductivity [3] in the nanoscale LiF/M framework can also affect the value and shape of the reaction voltage.

3.3 Particle size and electrochemical electrode voltage

The conversion reaction of transition metal difluoride involves local phase nucleation and evolution during the lithiation process. Metal difluoride converts into metal nanoparticle and LiF phases during lithiation. In order to study the correlation of metal nanoparticle formation with conversion reaction voltage in the fully lithiated state, CuF_2/C and NiF_2/C were galvanostatically lithiated (Fig. S1 in the ESM). Various TEM/STEM techniques including SAED patterns, ADF-STEM images, and EELS spectra were used to study the structural and morphological changes of the CuF_2/C and NiF_2/C electrodes during lithiation. We have taken 15 different ADF-STEM images, EELS spectra, and 10 different SAED patterns from various regions of the samples and the representatives of the observed images,

EELS spectra, and SAED patterns are presented here. The bright contrasts in the ADF-STEM image (Fig. 3(a)) correspond to the areas where the highest concentration of Cu can be seen, as ADF-STEM image contrast is highly sensitive to atomic number (~$Z^{1.7}$).

The ADF-STEM image of the lithiated NiF_2/C in Fig. 3(b) shows the distribution of Ni nanoparticles (bright contrast) in a LiF matrix. It is observed that lithiated CuF_2/C and lithiated NiF_2/C are composed of Cu and Ni with average particle sizes of ~2.5 and ~1.5 nm, respectively. The particle size distributions of Cu and Ni were obtained from several ADF-STEM images shown in Figs. 3(c) and 3(d). The lithiated CuF_2/C contained broad particle size ranges from 1 to 10 nm whereas the lithiated NiF_2/C consisted of Ni particle sizes ranging from 1 to 5 nm. The distinction in average particle sizes is attributed to the differences in diffusion rates of Cu and Ni ions; Cu has a higher diffusivity and thus forms larger particles [14, 16]. The SAED patterns of the pristine CuF_2/C and NiF_2/C nanocomposites confirm the existence of a single phase with a monoclinic and tetragonal–rutile structure as shown in Figs. 4(a) and 4(b), respectively.

Upon lithiation, CuF_2/C with a monoclinic structure converts into a cubic structure consisting of metallic Cu and LiF (Fig. 4(c)). Similarly, NiF_2 with a tetragonal-rutile structure transforms into metallic Ni and LiF upon lithiation, presented in Fig. 4(d). The presence of LiF in lithiated CuF_2/C and NiF_2/C is further verified by the characteristic near-edge fine structure in the Li K-edge spectra (Fig. 4(e)).

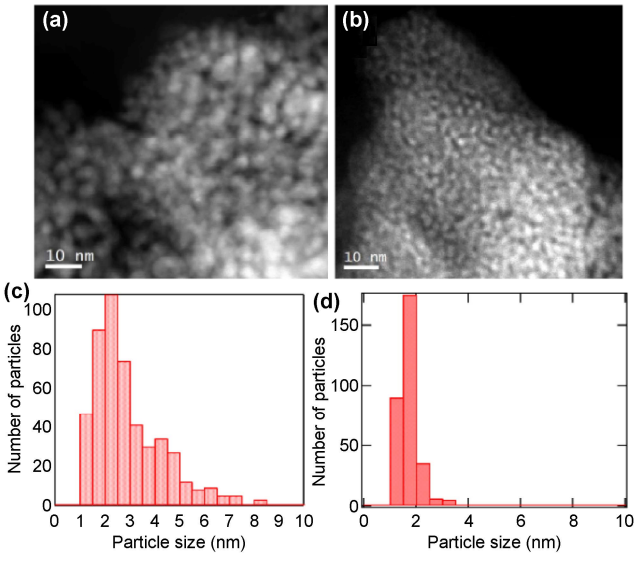

Figure 3 Representative ADF-STEM images of (a) lithiated CuF_2/C, and (b) lithiated NiF_2/C. The particle size distribution obtained from several ADF-STEM images of (c) lithiated CuF_2/C and (d) lithiated NiF_2/C.

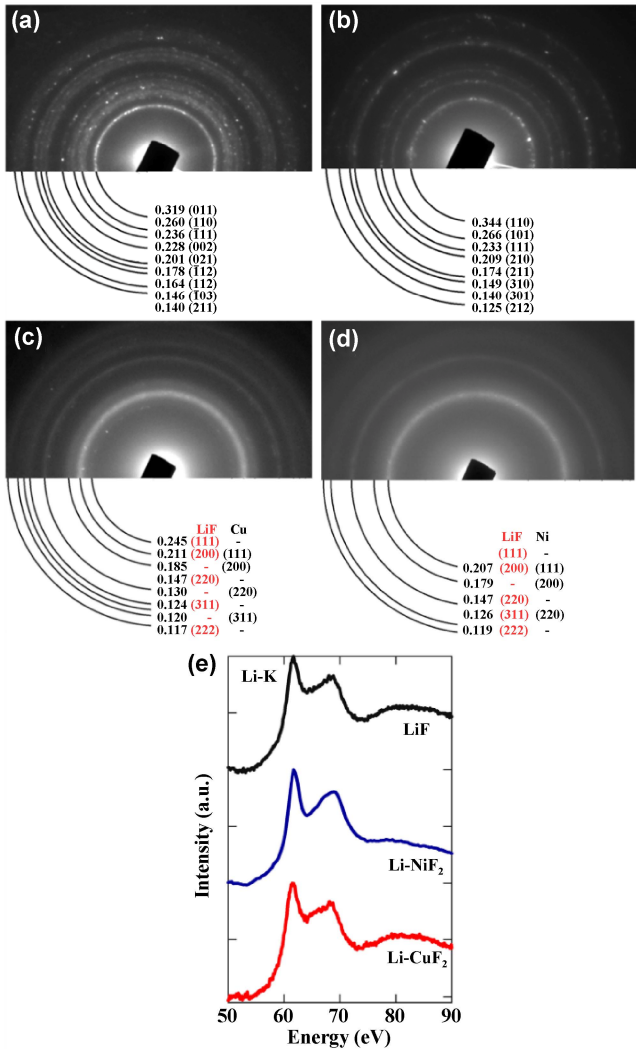

Figure 4 Representative SAED patterns of (a) pristine CuF_2/C, (b) pristine NiF_2/C, (c) lithiated CuF_2/C, (d) lithiated NiF_2/C, and (e) Li-K edge EELS spectra of the lithiated CuF_2/C (Li-CuF_2), lithiated NiF_2/C (Li-NiF_2), and reference LiF.

Interestingly, large Cu particles are found to be isolated and dispersed in the carbon matrix. Figure 5 shows the ADF image and the corresponding energy-dispersive X-ray (EDX) spectra of the lithiated CuF_2/C.

It is observed that large Cu particles (~10 nm) are distributed in the carbon matrix. This suggests that large Cu particles get isolated from LiF after the first discharge; therefore, they most probably have a

reduced chance to participate in the re-conversion reactions.

Additionally, PITT was applied to CuF_2/C and NiF_2/C cells to measure the conversion reaction voltages at a near-equilibrium state (Fig. 6).

This technique takes small voltage steps and monitors the current correlated with the reaction. We applied a voltage step of 10 mV. The voltage step does not proceed to the next step until the discharge current declines to a current limit of −1.1 and −1.3 μA for CuF_2/C and NiF_2/C cells, respectively (*C*/1,000 for both cells). PITT takes ~ 765 and ~ 909 hours for the first discharge of CuF_2/C and NiF_2/C, respectively. In the case of CuF_2/C, the open circuit voltage (OCV) was 3.09 V and the conversion reaction proceeded without any significant current decrease to the current limit at 3.02 V (Fig. 6(a)). The reaction continued at the following voltage steps with shortening plateaus. NiF_2/C had an OCV of 3.07 V and the conversion reaction initiated at 1.77 V after a rapid voltage drop (Fig. 6(b)). From our PITT results, we confirmed that the conversion reactions of both CuF_2/C and NiF_2/C occur at lower voltages than the thermodynamic bulk-reaction voltages ($E^{bulk}_{theoretical}$ (CuF_2) = 3.55 V and

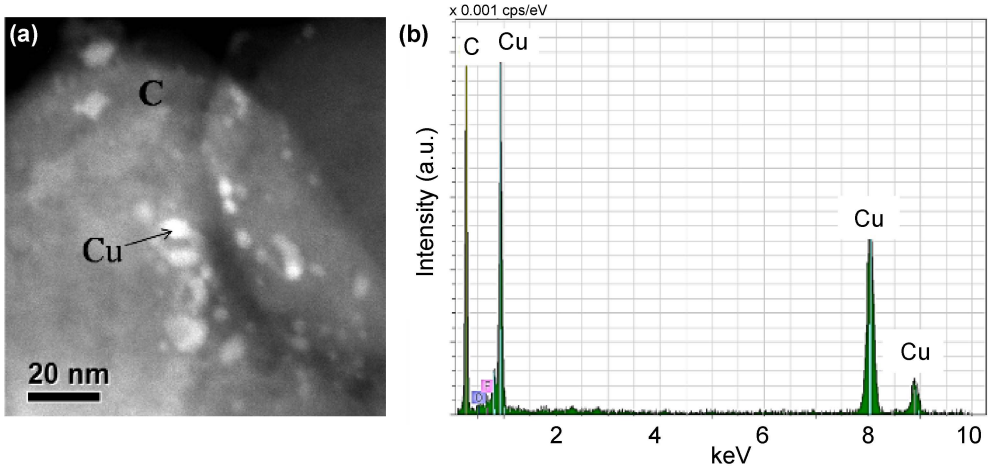

Figure 5 (a) Representative ADF-STEM and (b) EDX spectrum of the lithiated CuF_2/C showing the presence of large Cu metal (about 10 nm) on carbon matrix.

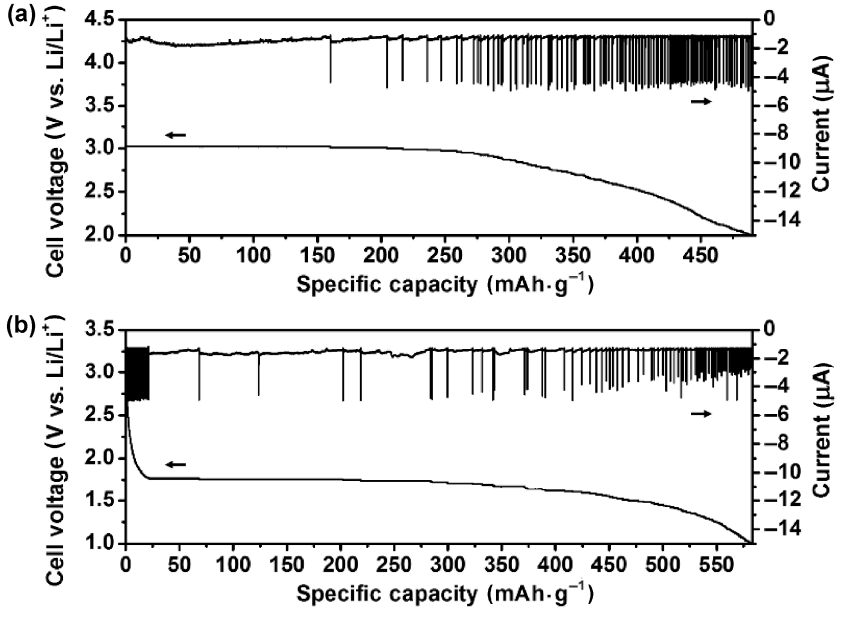

Figure 6 PITT discharges of (a) CuF_2/C and (b) NiF_2/C.

$E^{bulk}_{theoretical}$ (NiF_2) = 2.96 V). The formation of metal nanoparticles has a strong influence on the conversion voltage which is lower than the thermodynamic voltage of the bulk-phase reaction.

3.4 Rechargeable behavior of NiO-CuF_2 conversion material

According to previous reports, two main factors can result in a poor cycling performance of CuF_2: (i) Cu dissolution within the operating voltage window (2.0–4.0 V) [16], and (ii) isolated large Cu particle formation upon lithiation [14]. The linear potential sweep voltammogram for Cu demonstrates that Cu dissolves at ~3.5 V within the operating voltage window of the CuF_2 electrode (Fig. S2 in the ESM). In addition, our ADF-STEM images exhibited a bimodal Cu particle size distribution (Figs. 3(a) and 5(a)). The small Cu particles (~2.5 nm in average) were distributed in the microstructure of LiF (Fig. 3(a)), which is similar to observations made for other conversion materials including FeF_2 [48, 49]. However, the large Cu particles (~10 nm) were segregated from LiF and located in the carbon matrix (Fig. 5(a)). It is noteworthy that based on our ADF-STEM image, the majority of Cu particles were observed to be small (~2.5 nm in average) and embedded in LiF (Fig. 3(a)). This contrasts with the previous TEM work on CuF_2, which showed that only isolated large Cu particles (5–12 nm) formed upon lithiation [14].

CuF_2 is intrinsically a non-reversible conversion material, in contrast to FeF_2 and NiF_2. However, it has the highest thermodynamic voltage with a theoretical specific capacity of 528 mAh·g^{-1}. In the present work, we developed a novel reversible NiO-CuF_2/C electrode. Figure 7 shows the electrochemical voltage profile of CuF_2/C and NiO-CuF_2/C electrodes in the voltage window in the range 2.0–4.0 V at a *C*/35 rate.

CuF_2/C delivered a discharge capacity of 303 mAh·g^{-1} (57% of theoretical capacity). Similarly, the NiO-CuF_2/C electrode shows a first discharge capacity of 323 mAh·g^{-1} (61% of the theoretical capacity). Both electrodes show quite low voltage plateaus (2.75 and 2.77 V for NiO-CuF_2/C and CuF_2/C, respectively) compared to the thermodynamic voltage of the bulk-phase reaction (3.55 V). However, the NiO-CuF_2/C electrode displays a reversible conversion reaction with specific capacity

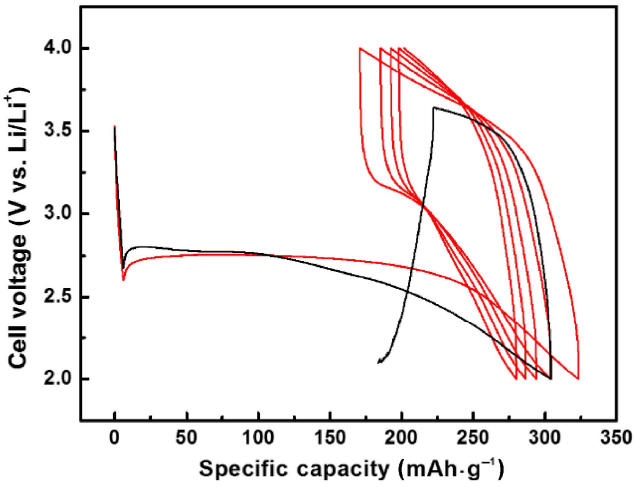

Figure 7 Voltage profiles of CuF_2/C and NiO-CuF_2/C electrodes.

of 152 mAh·g^{-1} during the first charge. During the charging process, the CuF_2/C electrode voltage starts to drop from ~3.64 V resulting in a charge failure. We ascribe this to Cu^{2+} dissolution from the cathode.

In order to gain in-depth insights into the effects of NiO on CuF_2 reversibility, the distribution of Cu and Ni in the lithiated NiO-CuF_2/C sample was studied using STEM-EELS elemental mapping. As lithium and fluoride-based compounds are extremely beam sensitive, we optimized the electron dose and spatial resolution to minimize the beam damage in this work. As such, the STEM-EELS spectrum image is taken with a total electron dose of 3×10^4 e·nm^{-2}. A representative ADF-STEM image and the corresponding Cu-$L_{2,3}$, and Ni-$L_{2,3}$ edge elemental maps are shown in Fig. 8.

It is observed that the bright contrast is attributed to the areas with the highest concentration of Cu. It is interesting that Ni-rich areas are located in the same regions as Cu-rich areas. It also indicates that the lithiation process mostly occurs in areas with high NiO content. We propose NiO as an artificial solid electrolyte interphase (SEI). NiO is an insoluble solid phase and is electrochemically inactive within the voltage window (2.0–4.0 V), which reduces the direct contact between the cathode and the electrolyte, and possibly alleviates Cu dissolution in the electrolyte. It has been reported that metal oxides could suppress metal ion dissolution into the electrolyte [50–52]. In addition, large Cu particles (~10 nm) are observed in the carbon matrix in the first-time discharged NiO-CuF_2/C. Our ADF-STEM and the corresponding EELS

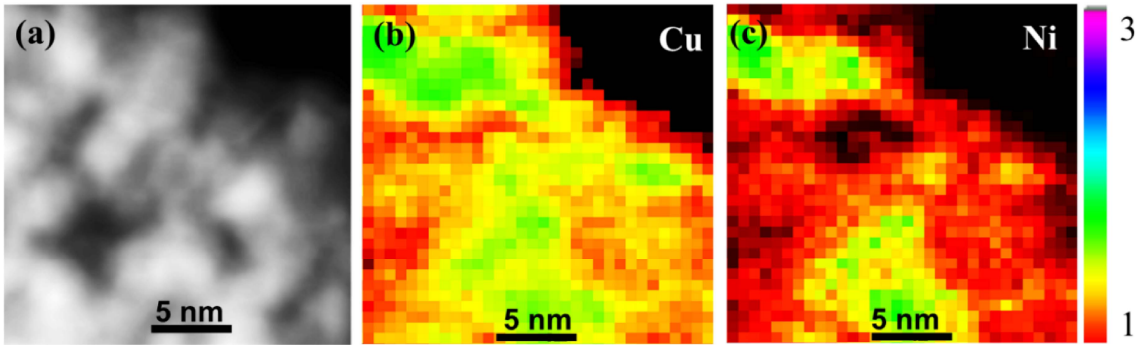

Figure 8 Representative ADF-STEM image of (a) the first discharged NiO-CuF_2/C and the corresponding elemental maps for (b) Cu-L, and (c) Ni-L.

spectra of the first-time discharged NiO-CuF_2/C (Figs. S3(a), S3(c), and S3(d) in the ESM) showed the presence of large Cu particles (~10 nm) distributed in the carbon matrix, similar to what was found from the lithiated CuF_2/C (Fig. 5(a)). Interestingly, the large Cu particles were still present in the first-time charged NiO-CuF_2/C (Figs. S3(b), S3(e), S3(f) in the ESM). This implies that large Cu particles in the carbon domain have less opportunity to participate in further cycles.

To investigate the extent of Cu dissolution into the electrolyte, elemental analysis of the electrolyte was performed using ICP-OES. The first cycled (discharge/charge) CuF_2/C and NiO-CuF_2/C cells were disassembled and their electrolytes collected. It is noted that CuF_2/C cell cannot be charged up to 4 V because of its non-reversible feature in contrast with the NiO-CuF_2/C cell. For that reason, the electrolyte from the CuF_2/C cell was collected after the CuF_2/C cell failed during the charging process. We found that Cu dissolution into the electrolyte was alleviated when the electrode was coated with NiO (Fig. S4 in the ESM). The concentration of Cu in the electrolyte when using CuF_2 electrode was measured to be ~13 ppb; however, the NiO-CuF_2 electrode shows a Cu concentration of ~0 ppb. This observation directly indicates that NiO coating suppresses Cu dissolution and alleviates electrode degradation.

Recently, a bimodal-size evolution of Ni nanoparticles from NiO-NiF_2/C electrode has been reported by pair distribution function (PDF) analysis, and that NiO possibly facilitates the conversion process by providing electronic conductivity [3]. The NiF_2/C electrode, however, is only converted into smaller Ni nanoparticles because of its insulating property. In order to investigate the phase transformation in CuF_2/C and NiO-CuF_2/C, we also conducted PDF for (a) first-time discharged CuF_2/C, (b) first-time discharged NiO-CuF_2/C, (c) first-time charged NiO-CuF_2/C, and (d) second-time discharged NiO-CuF_2/C samples, as shown in Fig. S5 in the ESM. We measured the Cu phase with average nanoparticle size of ~2.3 nm from the second-time discharged NiO-CuF_2/C (Fig. S5(d) in the ESM). Cu_2O are mainly found from the other samples instead of the Cu phase (Figs. S5(a)–S5(c) in the ESM), which is most likely to have resulted from the contamination of samples by air when they were kept in Kapton capillaries [16]. Although more PDF work is needed, our PDF refinement on the second-time discharged NiO-CuF_2/C confirms the formation of Cu nanoparticles, which suggests that NiO facilitates the CuF_2/C reversible reaction.

4 Conclusions

In this study, we combined first principles calculations and experiments with characterization techniques to analyze the conversion reaction voltage for MF_2(M = Fe, Ni, Cu) in Li-ion batteries. Based on our calculations, the voltage heavily depends on the size of metal nanoparticle generated. The formation of metal nanoparticles affects the conversion reaction voltage, which is lower than the thermodynamic voltage of the bulk-phase reaction. We propose that the surface energy of metal nanoparticle is an energy penalty against the free energy of reaction, bringing about a reduced voltage. Our ADF-STEM images demonstrated Cu and Ni

nanoparticle formations for the first discharged CuF_2 and NiF_2, respectively. Similarly, the PITT results show that the conversion reactions of CuF_2 and NiF_2 occur at lower voltages as a result of metal nanoparticle formation.

Moreover, we developed a rechargeable CuF_2 electrode by introducing NiO. We propose that NiO reduces the immediate contact between the CuF_2 and the electrolyte, thus suppressing Cu dissolution. We suggest that NiO can be used as an artificial SEI layer to improve the reversibility of Cu-based conversion materials. Further research on surface coatings will provide a breakthrough in the class of high energy density conversion materials.

Acknowledgements

M. S. and Y. S. M. gratefully acknowledge the funding support from the Office of Vehicle Technologies, U.S. Department of Energy under Contract No. DE-AC02-05CH11231, Subcontract No. 7073923 under the Advanced Battery Materials Research (BMR) Program. We use facilities of Extreme Science and Engineering Discovery Environment (XSEDE), which is supported by National Science Foundation (No. ACI-1053575). The TEM/STEM work is done at National Center of Electron Microscopy, Lawrence Berkeley National Laboratory and Rutgers University IAMDN. Our PDF work is done at Advanced Photon Sources of Argonne National Laboratory, Office of Science User Facility operated for the U.S. Department of Energy, Office of Science, supported by the U.S. Department of Energy (No. DE-AC02-06CH11357).

Electronic Supplementary Material: Supplementary material (further details of average radius of nanoparticle, bulk-phase reaction voltages, comparison of lattice parameters, the first discharge curves, linear potential sweep voltammogram, ADF-STEM images and EELS spectra, ICP-OES data, and experimental PDF profiles) is available in the online version of this article at http://dx.doi.org/10.1007/s12274-016-1365-6.

References

[1] Armstrong, M. J.; O'Dwyer, C.; Macklin, W. J.; Holmes, J. D. Evaluating the performance of nanostructured materials as lithium-ion battery electrodes. *Nano Res.* **2014**, *7*, 1–62.

[2] Cabana, J.; Monconduit, L.; Larcher, D.; Palacín, M. R. Beyond intercalation-based Li-ion batteries: The state of the art and challenges of electrode materials reacting through conversion reactions. *Adv. Mater.* **2010**, *22*, E170–E192.

[3] Lee, D. H.; Carroll, K. J.; Chapman, K. W.; Borkiewicz, O. J.; Calvin, S.; Fullerton, E. E.; Meng, Y. S. Understanding improved electrochemical properties of NiO-doped NiF_2-C composite conversion materials by X-ray absorption spectroscopy and pair distribution function analysis. *Phys. Chem. Chem. Phys.* **2014**, *16*, 3095–3102.

[4] Badway, F.; Pereira, N.; Cosandey, F.; Amatucci, G. G. Carbon-metal fluoride nanocomposites structure and electrochemistry of FeF_3:C. *J. Electrochem. Soc.* **2003**, *150*, A1209–A1218.

[5] Badway, F.; Cosandey, F.; Pereira, N.; Amatucci, G. G. Carbon metal fluoride nanocomposites: High-capacity reversible metal fluoride conversion materials as rechargeable positive electrodes for Li batteries. *J. Electrochem. Soc.* **2003**, *150*, A1318–A1327.

[6] Badway, F.; Mansour, A. N.; Pereira, N.; Al-Sharab, J. F.; Cosandey, F.; Plitz, I.; Amatucci, G. G. Structure and electrochemistry of copper fluoride nanocomposites utilizing mixed conducting matrices. *Chem. Mater.* **2007**, *19*, 4129–4141.

[7] Gocheva, I. D.; Tanaka, I.; Doi, T.; Okada, S.; Yamaki, J.-I. A new iron oxyfluoride cathode active material for Li-ion battery, Fe_2OF_4. *Electrochem. Commun.* **2009**, *11*, 1583–1585.

[8] Pereira, N.; Badway, F.; Wartelsky, M.; Gunn, S.; Amatucci, G. G. Iron oxyfluorides as high capacity cathode materials for lithium batteries. *J. Electrochem. Soc.* **2009**, *156*, A407–A416.

[9] Wiaderek, K. M.; Borkiewicz, O. J.; Castillo-Martínez, E.; Robert, R.; Pereira, N.; Amatucci, G. G.; Grey, C. P.; Chupas, P. J.; Chapman, K. W. Comprehensive insights into the structural and chemical changes in mixed-anion FeOF electrodes by using operando PDF and NMR spectroscopy. *J. Am. Chem. Soc.* **2013**, *135*, 4070–4078.

[10] Cosandey, F.; Su, D.; Sina, M.; Pereira, N.; Amatucci, G. G. Fe valence determination and Li elemental distribution in lithiated $FeO_{0.7}F_{1.3}$/C nanocomposite battery materials by electron energy loss spectroscopy (EELS). *Micron* **2012**, *43*, 22–29.

[11] Wang, F.; Kim, S.-W.; Seo, D.-H.; Kang, K.; Wang, L. P.; Su, D.; Vajo, J. J.; Wang, J.; Graetz, J. Ternary metal fluorides as high-energy cathodes with low cycling hysteresis. *Nat. Commun.* **2015**, *6*, 6668.

[12] Li, H.; Balaya, P.; Maier, J. Li-storage via heterogeneous reaction in selected binary metal fluorides and oxides. *J.*

Electrochem. Soc. **2004**, *151*, A1878–A1885.

[13] Ko, J. K.; Wiaderek, K. M.; Pereira, N.; Kinnibrugh, T. L.; Kim, J. R.; Chupas, P. J.; Chapman, K. W.; Amatucci, G. G. Transport, phase reactions, and hysteresis of iron fluoride and oxyfluoride conversion electrode materials for lithium batteries. *ACS Appl. Mater. Interfaces* **2014**, *6*, 10858–10869.

[14] Wang, F.; Robert, R.; Chernova, N. A.; Pereira, N.; Omenya, F.; Badway, F.; Hua, X.; Ruotolo, M.; Zhang, R. G.; Wu, L. J. et al. Conversion reaction mechanisms in lithium ion batteries: Study of the binary metal fluoride electrodes. *J. Am. Chem. Soc.* **2011**, *133*, 18828–18836.

[15] Lee, D. H.; Carroll, K. J.; Calvin, S.; Jin, S.; Meng, Y. S. Conversion mechanism of nickel fluoride and NiO-doped nickel fluoride in Li ion batteries. *Electrochim. Acta* **2012**, *59*, 213–221.

[16] Yamakawa, N.; Jiang, M.; Grey, C. P. Investigation of the conversion reaction mechanisms for binary copper(II) compounds by solid-state NMR spectroscopy and X-ray diffraction. *Chem. Mater.* **2009**, *21*, 3162–3176.

[17] Hua, X.; Robert, R.; Du, L.-S.; Wiaderek, K. M.; Leskes, M.; Chapman, K. W.; Chupas, P. J.; Grey, C. P. Comprehensive study of the CuF_2 conversion reaction mechanism in a lithium ion battery. *J. Phys. Chem. C* **2014**, *118*, 15169–15184.

[18] Towns, J.; Cockerill, T.; Dahan, M.; Foster, I.; Gaither, K.; Grimshaw, A.; Hazlewood, V.; Lathrop, S.; Lifka, D.; Peterson, G. D. et al. Xsede: Accelerating scientific discovery. *Comput. Sci. Eng.* **2014**, *16*, 62–74.

[19] Kresse, G.; Furthmüller, J. Efficient iterative schemes for *ab initio* total-energy calculations using a plane-wave basis set. *Phys. Rev. B* **1996**, *54*, 11169–11186.

[20] Dudarev, S. L.; Botton, G. A.; Savrasov, S. Y.; Humphreys, C. J.; Sutton, A. P. Electron-energy-loss spectra and the structural stability of nickel oxide: An LSDA+U study. *Phys. Rev. B* **1998**, *57*, 1505–1509.

[21] Perdew, J. P.; Burke, K.; Ernzerhof, M. Generalized gradient approximation made simple. *Phys. Rev. Lett.* **1996**, *77*, 3865–3868.

[22] Blöchl, P. E. Projector augmented-wave method. *Phys. Rev. B* **1994**, *50*, 17953–17979.

[23] Kresse, G.; Joubert, D. From ultrasoft pseudopotentials to the projector augmented-wave method. *Phys. Rev. B* **1999**, *59*, 1758–1775.

[24] Kresse, G.; Furthmüller, J. Efficiency of *ab-initio* total energy calculations for metals and semiconductors using a plane-wave basis set. *Comput. Mater. Sci.* **1996**, *6*, 15–50.

[25] Jain, A.; Hautier, G.; Ong, S. P.; Moore, C. J.; Fischer, C. C.; Persson, K. A.; Ceder, G. Formation enthalpies by mixing GGA and GGA + *U* calculations. *Phys. Rev. B* **2011**, *84*, 045115.

[26] Cho, H.-M.; Chen, M. V.; MacRae, A. C.; Meng, Y. S. Effect of surface modification on nano-structured $LiNi_{0.5}Mn_{1.5}O_4$ spinel materials. *ACS Appl. Mater. Interfaces* **2015**, *7*, 16231–16239.

[27] Seo, J. K.; Khetan, A.; Seo, M. H.; Kim, H.; Han, B. First-principles thermodynamic study of the electrochemical stability of Pt nanoparticles in fuel cell applications. *J. Power Sources* **2013**, *238*, 137–143.

[28] Noh, S. H.; Han, B.; Ohsaka, T. First-principles computational study of highly stable and active ternary PtCuNi nanocatalyst for oxygen reduction reaction. *Nano Res.* **2015**, *8*, 3394–3403.

[29] Vitos, L.; Ruban, A. V.; Skriver, H. L.; Kollár, J. The surface energy of metals. *Surf. Sci.* **1998**, *411*, 186–202.

[30] Baletto, F.; Ferrando, R. Structural properties of nanoclusters: Energetic, thermodynamic, and kinetic effects. *Rev. Mod. Phys.* **2005**, *77*, 371–423.

[31] Yacamán, M. J.; Ascencio, J. A.; Liu, H. B.; Gardea-Torresdey, J. Structure shape and stability of nanometric sized particles. *J. Vac. Sci. Technol. B* **2001**, *19*, 1091–1103.

[32] Noh, S. H.; Seo, M. H.; Seo, J. K.; Fischer, P.; Han, B. First principles computational study on the electrochemical stability of Pt-Co nanocatalysts. *Nanoscale* **2013**, *5*, 8625–8633.

[33] Escaño, M. C. S. First-principles calculations of the dissolution and coalescence properties of Pt nanoparticle ORR catalysts: The effect of nanoparticle shape. *Nano Res.* **2015**, *8*, 1689–1697.

[34] Klabunde, K. J.; Richards, R. M. *Nanoscale Materials in Chemistry*; 2nd ed.; John Wiley & Sons, Inc.: Hoboken, 2009.

[35] Wang, Z. L. Transmission electron microscopy of shape-controlled nanocrystals and their assemblies. *J. Phys. Chem. B* **2000**, *104*, 1153–1175.

[36] Li, Z. Y.; Young, N. P.; Di Vece, M.; Palomba, S.; Palmer, R. E.; Bleloch, A. L.; Curley, B. C.; Johnston, R. L.; Jiang, J.; Yuan, J. Three-dimensional atomic-scale structure of size-selected gold nanoclusters. *Nature* **2008**, *451*, 46–48.

[37] Yamakawa, N.; Jiang, M.; Key, B.; Grey, C. P. Identifying the local structures formed during lithiation of the conversion material, iron fluoride, in a Li ion battery: A solid-state NMR, X-ray diffraction, and pair distribution function analysis study. *J. Am. Chem. Soc.* **2009**, *131*, 10525–10536.

[38] Mansour, A. N.; Badway, F.; Yoon, W.-S.; Chung, K. Y.; Amatucci, G. G. *In situ* X-ray absorption spectroscopic investigation of the electrochemical conversion reactions of CuF_2–MoO_3 nanocomposite. *J. Solid State Chem.* **2010**, *183*, 3029–3038.

[39] Curtarolo, S.; Morgan, D.; Persson, K.; Rodgers, J.; Ceder, G. Predicting crystal structures with data mining of quantum calculations. *Phys. Rev. Lett.* **2003**, *91*, 135503.

[40] Barin, I.; Sauert, F.; Schultze-Rhonhof, E.; Sheng, W. S. *Thermochemical Data of Pure Substances*; VCH: Weinheim, 1993.

[41] Liu, P.; Vajo, J. J.; Wang, J. S.; Li, W.; Liu, J. Thermodynamics and kinetics of the Li/FeF_3 reaction by electrochemical analysis. *J. Phys. Chem. C* **2012**, *116*, 6467–6473.

[42] Poizot, P.; Laruelle, S.; Grugeon, S.; Dupont, L.; Tarascon, J. M. Nano-sized transition-metal oxides as negative-electrode materials for lithium-ion batteries. *Nature* **2000**, *407*, 496–499.

[43] Lin, C.-F.; Noked, M.; Kozen, A. C.; Liu, C. Y.; Zhao, O.; Gregorczyk, K.; Hu, L. B.; Lee, S. B.; Rubloff, G. W. Solid electrolyte lithium phosphous oxynitride as a protective nanocladding layer for 3D high-capacity conversion electrodes. *ACS Nano* **2016**, *10*, 2693–2701.

[44] Medasani, B.; Park, Y. H.; Vasiliev, I. Theoretical study of the surface energy, stress, and lattice contraction of silver nanoparticles. *Phys. Rev. B* **2007**, *75*, 235436.

[45] Delmer, O.; Balaya, P.; Kienle, L.; Maier, J. Enhanced potential of amorphous electrode materials: Case study of RuO_2. *Adv. Mater.* **2008**, *20*, 501–505.

[46] Liao, P.; Dunlap, R. A.; Dahn, J. R. A mössbauer effect study of combinatorially prepared Al_2O_3/Fe and LiF/Fe multilayers. *J. Phys.: Condens. Matter* **2008**, *20*, 055203.

[47] Dalverny, A. L.; Filhol, J. S.; Doublet, M. L. Interface electrochemistry in conversion materials for Li-ion batteries. *J. Mater. Chem.* **2011**, *21*, 10134–10142.

[48] Sina, M.; Thorpe, R.; Rangan, S.; Pereira, N.; Bartynski, R. A.; Amatucci, G. G.; Cosandey, F. Investigation of SEI layer formation in conversion iron fluoride cathodes by combined STEM/EELS and XPS. *J. Phys. Chem. C* **2015**, *119*, 9762–9773.

[49] Rangan, S.; Thorpe, R.; Bartynski, R. A.; Sina, M.; Cosandey, F.; Celik, O.; Mastrogiovanni, D. D. T. Conversion reaction of FeF_2 thin films upon exposure to atomic lithium. *J. Phys. Chem. C* **2012**, *116*, 10498–10503.

[50] Cho, J.; Kim, T.-J.; Park, B. The effect of a metal-oxide coating on the cycling behavior at 55°C in orthorhombic $LiMnO_2$ cathode materials. *J. Electrochem. Soc.* **2002**, *149*, A288–A292.

[51] Kim, B.; Lee, J.-G.; Choi, M.; Cho, J.; Park, B. Correlation between local strain and cycle-life performance of $AlPO_4$-coated $LiCoO_2$ cathodes. *J. Power Sources* **2004**, *126*, 190–192.

[52] Shin, J.; You, J.-M.; Lee, J. Z.; Kumar, R.; Yin, L.; Wang, J.; Meng, Y. S. Deposition of ZnO on bismuth species towards a rechargeable Zn-based aqueous battery. *Phys. Chem. Chem. Phys.* **2016**, 18, 26376–26382.

Table of contents

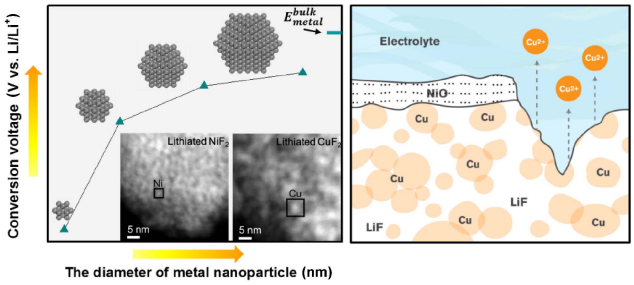

The conversion reaction voltage in the Li ion battery is reinterpreted based on the size of metal nanoparticles. A reversible CuF_2 electrode is developed by coating with NiO.

Electronic Supplementary Material

Revisiting the conversion reaction voltage and the reversibility of the CuF_2 electrode in Li-ion batteries

Joon Kyo Seo[1,2], Hyung-Man Cho[1,2], Katsunori Takahara[1], Karena W. Chapman[3], Olaf J. Borkiewicz[3], Mahsa Sina[1] (✉), and Y. Shirley Meng[1,2] (✉)

[1] *Department of NanoEngineering, University of California San Diego, 9500 Gilman Drive, La Jolla, CA 92093, USA*
[2] *Materials Science and Engineering, University of California San Diego, 9500 Gilman Drive, La Jolla, CA 92093, USA*
[3] *X-ray Science Division, Advanced Photon Source, Argonne National Laboratory, 9700 South Cass Avenue, Argonne, IL 60439, USA*

Supporting information to DOI 10.1007/s12274-016-1365-6

Table S1 Comparison of lattice parameters between GGA + *U* calculation and experiments

	Compund	*a* (Å)	*b* (Å)	*c* (Å)	*β* (°)
GGA + *U* calculation	CuF_2	3.32 (1.06%)	4.617 (1.20%)	4.671 (1.19%)	82.756 (0.65%)
	NF_2	4.696 (1.00%)	4.696 (1.00%)	3.104 (0.67%)	90.0000
	FeF_2	4.788 (1.99%)	4.788 (1.99%)	3.3.16 (0.18%)	90.0000
Experimental	CuF_2	3.297	4.562	4.616	83.293
	NF_2	4.650	4.650	3.084	90.0000
	FeF_2	4.695	4.695	3.310	90.0000

We adopt *U* as 4.0, 6.0, and 4.0 for Fe, Ni, and Cu, respectively [S1]. The percentage in parenthesis shown in Table S1 represents the deviation ratio of lattice parameters calculated from GGA + *U* calculation, with respect to experimental data [S2, S3].

Table S2 The average radius of M (M = Fe, Ni, and Cu) nanoparticle composed of *n* atoms

n	Iron		Nickel		Copper	
	Cubotahedron	Icosahedron	Cuboctahedron	Icosahedron	Cuboctahedron	Icosahedron
13	2.44 Å	2.40 Å	2.37 Å	2.32 Å	2.47 Å	2.41 Å
55	4.85 Å	4.75 Å	4.80 Å	4.60 Å	4.94 Å	4.81 Å
147	7.25 Å	7.04 Å	7.26 Å	7.01 Å	7.49 Å	7.29 Å
309	9.94 Å	9.30 Å	9.71 Å	9.39 Å	10.03 Å	9.74 Å

Address correspondence to Y. Shirley Meng, shmeng@ucsd.edu; Mahsa Sina, msina@ucsd.edu

All nanoparticle morphologies are fully relaxed. The average distance between the center and vertex atoms is defined as a radius of M (M = Fe, Ni, and Cu) nanoparticle composed of *n* atoms shown in Table S2.

Table S3 Bulk-phase reaction voltages calculated from GGA, mixing GGA/GGA + *U*, and Gibbs free energy of formation in thermodynamic table

Method	FeF_2	NiF_2	CuF_2
GGA	3.06 V	3.46 V	3.70 V
Mixing GGA/GGA + *U* (this work)	2.58 V	2.91 V	3.56 V
Gibbs free energy and formation (thermaodynamic table)	2.66 V	2.96 V	3.55 V

The voltage calculated from mixing GGA/GGA + *U* shows less than 0.09 V difference compared to the voltage measured from thermodynamic table as shown in Table S3. GGA calculations, however, overestimate voltages up to ~ 0.50 V. Therefore we apply mixed GGA/GGA + *U* scheme throughout the study.

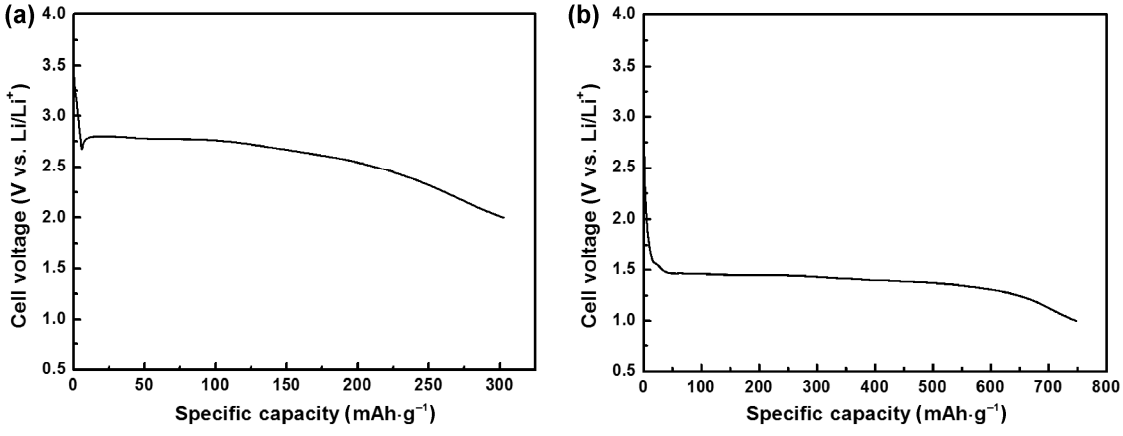

Figure S1 The first discharge of (a) CuF_2/C and (b) NiF_2/C.

The first discharge of CuF_2/C and NiF_2/C are tested with the constant current density of *C*/35. The voltage limit is 2.0 and 1.0 V for CuF_2/C and NiF_2/C, respectively.

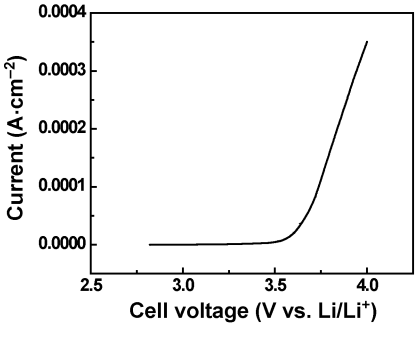

Figure S2 Linear potential sweep voltammogram for Cu foil.

Linear potential sweep voltammogram for Cu foil is conducted as shown in Fig. S2. Cu foil is employed for the working electrode. We use a pure lithium metal as a counter electrode and a polypropylene C480 (Celgard) as a separator. The coin cell (2016) is assembled with the electrolyte consisting of 1 M $LiPF_6$ dissolved in EC and DMC with a weight ratio of 1:1 (BASF) in the MBraun Ar-filled glovebox (H_2O < 0.1 ppm). A Solartron 1,287 electrochemical interface is used to perform the linear potential sweep voltammogram with the scan rate of 1 $mV \cdot s^{-1}$.

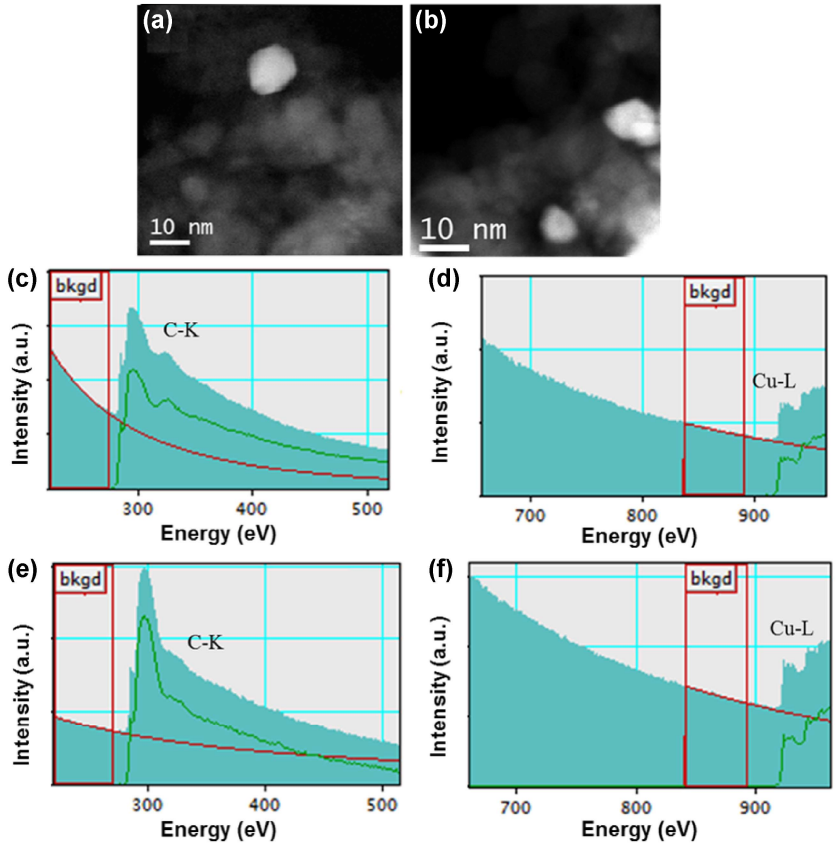

Figure S3 ADF-STEM of (a) the first discharged and (b) the first charged NiO-CuF_2/C. C-K edge EELS spectra of (c) the first discharged and (e) the first charged NiO-CuF_2/C. Cu-L edge EELS spectra of (d) the first discharged and (f) the first charged NiO-CuF_2/C.

Figure S3(a) exhibits the ADF-STEM image of the first discharged NiO-CuF_2, showing large copper particles with bright contrast in carbon matrix. The corresponding EELS spectra are displayed in Figs. S3(c) and S3(d), which confirms the presence of metallic copper and carbon, and nonexistence of F-K edge (around 690 eV) from LiF phase. The presence of large copper particles in carbon matrix can still be observed after the first charge (Figs. S3(b), S3(e), and S3(f)). This further validates that the large copper particles are isolated from LiF phase and do not participate in the first charge.

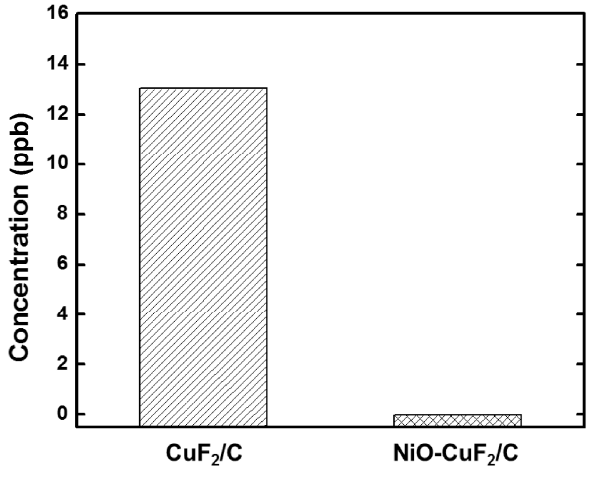

Figure S4 Cu dissolution into the electrolyte from CuF_2/C and NiO-CuF_2/C electrodes.

Cu dissolution is measured by ICP-OES as shown in Fig. S4. A custom-made cell consisting of a CuF_2/C (or NiO-CuF_2/C), a pure lithium metal, a polypropylene C480 (Celgard) is assembled with 1 M $LiPF_6$ dissolved in EC and DMC with a weight ratio of 1:1 (BASF) in the MBraun Ar-filled glovebox (H_2O < 0.1 ppm). The first cycled (discharge/charge) CuF_2/C and NiO-CuF_2/C cells are disassembled and the electrolyte is collected to perform ICP-OES.

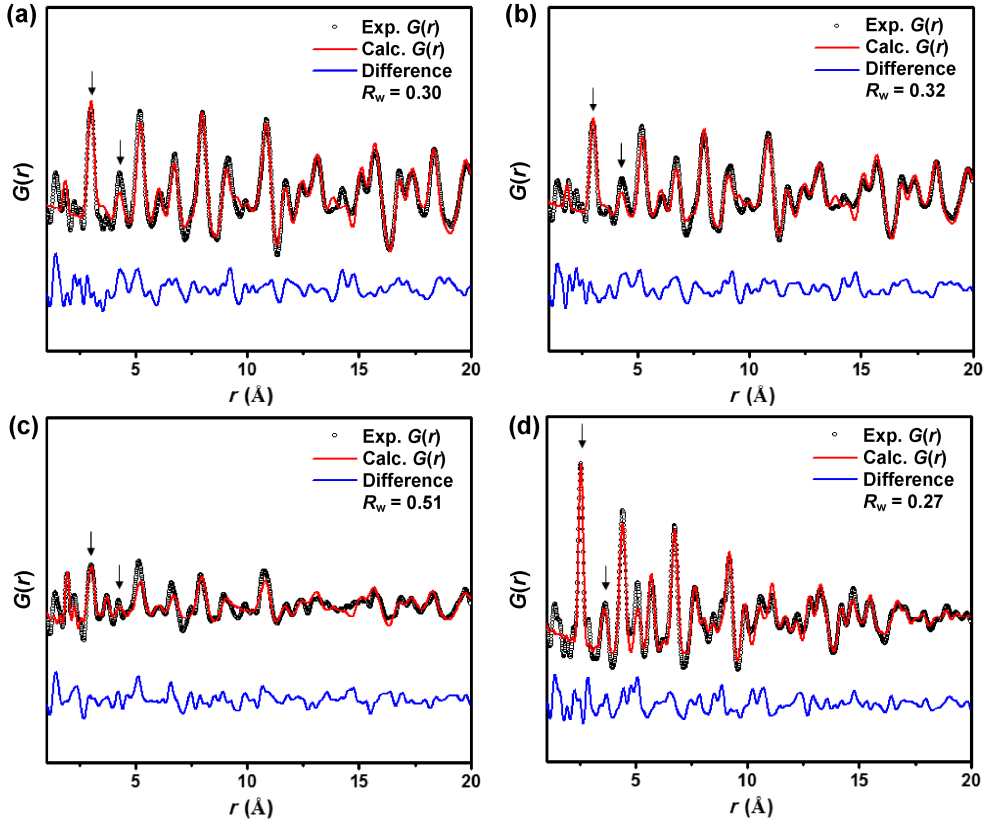

Figure S5 Experimental PDF (Exp. $G(r)$), refined fit (Calc. $G(r)$), and difference between Exp. $G(r)$ and Calc. $G(r)$. (a) The first discharged CuF_2/C, (b) first discharged NiO-CuF_2/C, (c) first charged NiO-CuF_2/C, and (d) second discharged NiO-CuF_2/C.

We collect high-energy total X-ray scattering data (λ = 0.2114 Å) at the PDF beamline 11-ID-B of the Advanced Photon Source in Argonne National Laboratory as shown in Fig. S5. We integrate raw images by using the software FIT2d [S4]. PDFgetX2 [S5] is utilized to correct the data for background contributions, Compton scattering, and detector effects. Fourier transform is conducted to generate $G(r)$, the PDF. We refine PDF data using PDFgui [S6]. The electrode samples are (a) first discharged CuF_2/C, (b) first discharged NiO-CuF_2/C, (c) first charged NiO-CuF_2/C, and (d) second discharged NiO-CuF_2/C. CuF_2/C sample is discharged to 2 V, and NiO-CuF_2/C samples are discharged and charged to 2.0 and 4.0 V, respectively. Samples are obtained by disassembling the coin cells inside the Ar-filled glovebox. We wash electrodes with battery-grade DMC (Novolyte) and seal them in Kapton under Ar atmosphere.

The PDF analysis of X-ray total scattering data is applied to understand phase transformations during conversion reactions. The structural refinement on the first discharged CuF_2/C demonstrates the formation of Cu_2O. The peaks at 3.0 Å and 4.3 Å correspond to the first and second nearest Cu–Cu bonds in Cu_2O, respectively (Fig. S5 (a)). This phase has a cubic structure with the space group of $Pn\bar{3}m$. The PDF analysis for the first discharged and the first charged NiO-CuF_2/C also exhibits peaks at 3.0 Å and 4.3 Å representing Cu-Cu bonds in Cu_2O (FigS. S5(b) and S5(c)). The second discharged NiO-CuF_2/C indicates peaks at 2.6 and 3.6 Å

which are corresponding to the first and second nearest Cu–Cu bonds in Cu, respectively (Fig. S5(d)). Cu is a cubic structure with the space group of $Fm\bar{3}m$. The structural refinement on PDF for the second discharged NiO-CuF_2/C implies the formation of Cu nanoparticle with ~2.3 nm in diameter.

References

[S1] Jain, A.; Hautier, G.; Ong, S. P.; Moore, C. J.; Fischer, C. C.; Persson, K. A.; Ceder, G. Formation enthalpies by mixing GGA and GGA + *U* calculations. *Phys. Rev. B* **2011**, *84*, 045115.

[S2] Burns, P. C.; Hawthorne, F. C. Rietveld refinement of the crystal structure of CuF_2. *Powder Diffr.* **1991**, *6*, 156–158.

[S3] Baur, W. H.; Khan, A. A. Rutile-type compounds. IV. SiO_2, GeO_2 and a comparison with other rutile-type structures. *Acta Crystallogr. B: Struct. Sci. Cryst. Eng. Mater.* **1971**, *27*, 2133–2139.

[S4] Hammersley, A. P.; Svensson, S. O.; Hanfland, M.; Fitch, A. N.; Hausermann, D. Two-dimensional detector software: From real detector to idealised image or two-theta scan. *High Pressure Res.* **1996**, *14*, 235–248.

[S5] Qiu, X.; Thompson, J. W.; Billinge, S. J. L. *PDFgetX2*: A GUI-driven program to obtain the pair distribution function from X-ray powder diffraction data. *J. Appl. Crystallogr.* **2004**, *37*, 678.

[S6] Farrow, C. L.; Juhas, P.; Liu, J. W.; Bryndin, D.; Božin, E. S.; Bloch, J.; Proffen, T.; Billinge, S. J. L. PDFfit2 and PDFgui: Computer programs for studying nanostructure in crystals. *J. Phys.: Condens. Matter* **2007**, *19*, 335219.